Applied Catalysis B: Environmental 211 (2017) 137–147

Contents lists available at ScienceDirect

Applied Catalysis B: Environmental

journal homepage: www.elsevier.com/locate/apcatb

Zinc and platinum co-doped ceria for WGS and CO oxidation

Ravikiran Mandapaka, Giridhar Madras*

Department of Chemical Engineering, Indian Institute of Science, Bangalore, India

ARTICLE INFO

Article history:
Received 9 December 2016
Received in revised form 8 March 2017
Accepted 13 April 2017
Available online 15 April 2017

Keywords:
Co-doped catalysts
Microkinetics
Mechanism
Combustion synthesis

ABSTRACT

This study presents the synthesis and application of zinc and platinum co-doped ceria for CO oxidation and water gas shift reaction (WGS). To synthesize the catalyst, novel combustion synthesis procedure at pH = 10 has been employed, yielding the catalyst in single step without further purification procedures. The catalyst was found to be active under high temperature conditions (>350 °C) thus asserting the functionality of the catalyst as single stage WGS catalyst. In this study, we have also developed a dual site redox mechanism to understand the intrinsic kinetics of WGS reaction. For the proposed mechanism, a plausible microkinetic model has been developed for WGS and CO oxidation reactions, respectively. In line with the application of reaction route (RR) analysis to the microkinetic models developed for single site pathway for WGS. In this study, we have extended the RR approach to dual site redox mechanism. From the above analysis, the surface dissociation of OH surface species was found to be rate determining step of the mechanism. The rate expression developed using RR analysis was validated through isothermal plug flow reactor (PFR) model. The PFR simulations predicted the experimental trend for wider range of temperature conditions thus portraying the significance of the microkinetic model developed in this study.

1. Introduction

Water gas shift reaction (WGS) is a prominent reaction that occurs in many systems such as automotive exhaust abatement and hydrocarbon reforming [1,2]. Because of its moderate exothermicity of −41.2 kJ/mol, WGS is carried out in two stages namely low temperature shift reaction occurring at 150–300 °C and high temperature shift reaction occurring at 350–600 °C to increase the CO conversion. However, in recent years, with the advent of complex catalytic design procedures, the need for single stage WGS catalysts has become significant [3]. Ceria and noble metal combination catalysts have known to be active for WGS. Thus, ceria has been doped with Zr, Si, Al, Fe, Ti and bi metallic components [3–8]. It has also been shown that doping ceria with noble metals especially with platinum increases the WGS activity [4–7,9]. Doping ceria with divalent dopant of lower ionic radius increases the oxygen storage capacity (OSC) of the catalyst. Zinc doped ceria catalysts have been synthesized and used for various high temperature gas phase reactions such as WGS, CO oxidation, preferential oxidation and hydrocarbon oxidation [10–12] utilizing noble metal *i.e.*, Au and Pt, impregnation over ceria-zinc catalyst. However, the mechanism of WGS is complex and can be modeled by a wide variety of techniques.

Microkinetic models pertaining to WGS reaction propose mainly three mechanisms to be operational for WGS over noble metal catalysts *i.e.*, associative redox mechanism [4], formate mechanism [13] and carboxyl mechanism [14], respectively. The main difference between the mechanisms is the precedence of the reaction path involving various reaction intermediates such as formate and carboxyl surface species. In earlier studies, employing the reaction route analysis (RR) [13,15], a comprehensive rate expression has been developed for WGS involving a redox and modified redox mechanism occurring over metallic Cu site.

In this study, we present the comprehensive development of novel single stage catalyst for WGS and CO oxidation. We also present the extension of the RR approach to propose and validate a plausible microkinetic model developed for dual site redox mechanism for WGS over platinum and zinc co-doped ceria. The validity of the kinetic parameters and intrinsic rate expression developed for the proposed mechanism has been tested against the experimental results for this catalyst using different reactor approaches.

* Corresponding author.
E-mail addresses: giridhar@chemeng.iisc.ernet.in, giridharmadras@gmail.com (G. Madras).

http://dx.doi.org/10.1016/j.apcatb.2017.04.044
0926-3373/

2. Experimental section

2.1. Material synthesis

In this study, we have synthesized 5 at% Zn and 2 at% Pt in ceria. The synthesis procedures involving doping zinc in ceria reports the pH of precursor solution to be in the range of 7–9 [16–19]. This has been reported for sol-gel and solution combustion synthesis procedures as well. Similar procedure has been adopted in this study with a change in pH to prepare zinc and platinum co-doped ceria hereafter referred as CZPt and 2 at% Pt in ceria will be referred as CePt. The precursor solution consisting appropriate quantities of the precursors *i.e.*, zinc nitrate hexa hydrate [$(Zn(NO_3)_2.6H_2O$, Merck, India)], ammonium cerium nitrate [$(NH_4)_2Ce(NO_3)_6$, (Merck, India)], tetra amine platinum nitrate [$(H_{12}N_6O_6Pt)$, Alfa Aesar] and glycine [$C_2H_5NO_2$, (S.D. fine Chem, India)] pertaining to their relative substitution fractions were dissolved in 15 mL of D.I. water. The pH of the precursor solution was increased to 10 using 25% aqueous ammonia solution. This resulted in the gelation of the solution. The precursor solution was then transferred into a muffle furnace preheated at 400 °C. The solution boiled initially evaporating water and then ignited releasing voluminous release of product gases. The synthesis procedure resulted in the formation of porous solid, greyish brown in texture. The obtained catalyst was then calcined at 400 °C for 2 h and characterized using XRD, XPS, TEM and BET.

2.2. Material characterization

The X-ray diffraction (XRD) pattern was obtained using Rigaku X-ray diffraction equipment with Cu-kα, as the source of radiation. The obtained diffraction pattern was refined using Jana 2006 with 16 terms as the background function and pseudo-Voigt as peak shape function. The X-ray photoelectron spectra (XPS) of different elements was obtained using AXIS ULTRA instrument with Al-Kα, radiation source. For this, the segments of the pellets made from catalysts were stuck onto a carbon tape and were inserted into the Ultra high vacuum chamber of the instrument. Drop casting procedure was used to prepare TEM samples. The procedure briefly consists of dispersing the catalyst samples in methanol using ultrasonicator for 20 min. Then the solution was drop casted onto on carbon coated Cu grids (400 mesh size). TEM micrographs pertaining to CZPt was obtained using FEI Tecnai F30 instrument operated at 200 kV with point resolution of 0.24 nm and the spherical aberration of 1.2 mm. BET surface area of CZPt was measured using Belsorb® surface analyzer with liquid nitrogen as sorption medium to quantify the monolayer volume of the catalyst.

2.3. Experimental procedure for WGS and CO oxidation

In order to test the activity of the catalyst (CZPt) for WGS, different weights of the catalyst pellets (150–300 μm size) *i.e.*, 25 mg, 50 mg, 100 mg, 200 mg were diluted with silica beads and were loaded into the reactor *i.e.*, quartz tube (4 mm ID) to make a catalytic bed of 1 cm in length. The catalyst bed was held firmly at the center of the quartz tube using ceramic wool. CO and N_2 (99.9% purity) were passed into the quartz tube maintaining a volumetric flow rate of 100 mL/min (dry gas basis) with 2.0 vol % of CO and rest N_2. The water flow rate sent to the boiler was maintained at 0.05 mL/min. This corresponds to 65 mL/min in the gas phase. The steam from the boiler outlet was sent to the reactor. The excess unreacted steam in the exit gas was condensed using a moisture trap and the dry gas composition was analyzed using a gas chromatograph (Mayura Analytical Pvt. Ltd., India). The gas chromatograph consisted of a flame ionization detector (FID) for measuring the concentrations of CO, CO_2 and CH_4 and a thermal conductivity detector (TCD) to detect the concentrations of hydrogen. The temperature of the catalyst bed was maintained using a PID controlled heating furnace equipped with a thermocouple. The schematic of the experimental setup is given elsewhere [9]. The experimental procedure for CO oxidation is similar to WGS. Briefly, the inlet volume fraction of gaseous reactants was 2.4 vol % CO, 2.4 vol % O_2 and rest N_2 with inlet volumetric flow rate of 100 mL/min. The catalyst loading was varied as 15 mg, 50 mg and 75 mg.

2.4. H_2 TPR studies

10 mg of catalyst was taken in the center of quartz reactor. The inlet H_2 (5% H_2 rest Argon) flow rate to the reactor was maintained at 30 mL/min. The temperature of the catalyst was increased using a PID controlled furnace with a ramp rate of 10 °C/min. The reducibility of the catalyst was measured using the variation in the signal from the TCD detector. The H_2 consumption of the catalysts was calibrated using CuO (99.7% pure, Alfa Aesar).

3. Kinetic model development for CO oxidation and WGS mechanism

In line with the mechanism proposed in our earlier studies for CO oxidation over ionic catalysts, a 8-step dual site mechanism has been proposed in this study [20]. It is to be noted in the following study, Step i, denotes the forward reaction of ith surface reaction and step −i, denotes the backward reaction of ith surface reaction. Steps 1,-1 denotes the reversible CO adsorption on ionic platinum site. Steps 2,-2 represent dissociative O_2 adsorption on vacant site. Steps 3,-3 represent the surface reaction of adsorbed CO species and surface oxygen species; steps 4,-4 represent the surface desorption of CO_2.

$$\text{Step1, -1 : } CO + * \Leftrightarrow CO* \quad (1)$$

$$\text{Step2, -2 : } O_2 + 2v \Leftrightarrow 2[O] \quad (2)$$

$$\text{Step3, -3 : } [O] + CO* \Leftrightarrow CO_2* + v \quad (3)$$

$$\text{Step4, -4 : } CO_2* \Leftrightarrow CO_2 + * \quad (4)$$

In Eqs. (1)–(4), * denotes the ionic Pt site and 'v' denotes the vacancy.

3.1. Mechanisms for low temperature WGS

Different mechanisms for WGS have been proposed associated with different combinations of platinum-ceria duo for different feed conditions. In contrast to the conventional noble metal impregnated catalysts, noble metal ionic catalysts have shown superior activity and stability for WGS [9]. From the experimental data obtained for the activity of WGS reaction, it has been proposed that the reducible support plays a crucial role in determining the mechanism of WGS [21]. It has also been proposed that the reducible support is crucial for water molecule adsorption and surface water splitting reactions of the mechanism [22,23].

However, the mechanism of WGS for CZPt is similar to the mechanism of WGS on platinum impregnated on ceria involving the utilization of vacancies. The mechanism of WGS over Pt/ceria has been studied using various experimental techniques like diffuse reflectance infrared fourier transform spectroscopy (DRIFTS) [18,19,24–28], isotope switching studies [29] and steady state isotope exchange transient kinetic analysis (SSITKA) [24,30], X-ray absorption near edge spectroscopy [26], and density functional theory (DFT) [31–33], based calculations. In a broader prospective, three mechanisms have been proposed for WGS over Pt-impregnated ceria which are, redox mechanism, associative mechanism with formate intermediate and associative mechanism with carboxyl intermediate.

Briefly, the scheme of the redox mechanism can be briefly depicted as shown (* – adsorption site on Pt)

$$CO + * \Leftrightarrow CO* \quad (5)$$

$$CO* + 2CeO_2 \Leftrightarrow Ce_2O_3 + CO_2 + * \quad (6)$$

$$H_2O + Ce_2O_3 \Leftrightarrow H_2 + 2CeO_2 \quad (7)$$

The scheme of the associative mechanism (carboxyl/formate) on a single site can be briefly depicted as shown,

$$CO + * \Leftrightarrow CO* \quad (8)$$

$$H_2O + * \Leftrightarrow H_2O* \quad (9)$$

$$CO* + H_2O* \Leftrightarrow COOH* + H* \Leftrightarrow CO_2 + H_2 + 2* \quad (10)$$

(for carboxyl mechanism)

$$CO* + H_2O* \Leftrightarrow HCOO* + H* \Leftrightarrow CO_2 + H_2 + 2* \quad (11)$$

(for formate mechanism)

Evidence favoring each of the reaction mechanisms has been reported in literature and there is still no general consensus. The *in situ* DRIFTS studies report the formation of formate species by the reaction of CO with the OH groups of reduced ceria, which decomposes on addition of water. These studies also indicate that at low CO conversions, surface formates were limited as compared to metal-CO. This led to the conclusion that formate species would be decisive in the reaction mechanism [29].

The possibility of a redox process, involving cyclic oxidation and reduction of ceria utilizing its oxygen storage capacity, was investigated by Gorte and co-workers [34]. WGS rates were found to be similar for Pt/ceria, Pd/ceria and Rh/ceria. It was also found that large crystallites of ceria showed lesser WGS activity owing to their decreased reducibility. It has also been indicated the presence of carbonates on reduced ceria surface could be removed only be re-oxidizing the surface [34]. Only a redox mechanism was found to explain these observations. Stephanopoulos and co-workers [35] found that a co-operative redox mechanism fitted the WGS kinetics over Cu- and Ni- containing ceria. A more recent study using coupled quantitative DRIFTS and SSITKA also found redox mechanism to be the major pathway on Pt/ceria at temperatures around 300 °C [27].

Quantitative studies using *in situ* DRIFTS-MS-SSITKA conducted by Burch and co-workers [36] have shown that, upon isotope switch from ^{12}C to ^{13}C, the rate of exchange of formate is much slower than other reaction intermediates like carbonyl and carboxyl, and product CO_2. The formate pathway was found to account for about 10% of the CO_2 formed during WGS [37]. Recent *in situ* DRIFTS-MS-SSITKA studies conducted by Kalamaras et al. [27] also are in agreement with these observations. These conclusions are also reflected from DFT based calculations [31,32] that the formation of formate intermediate over Pt/ceria gives an activation barrier which is much higher than the barrier estimated to form a carboxyl intermediate indicating formate pathway to be unfavorable. Recently, a review of evidence for and against the formate mechanism was done by Burch et al. [38] and it was concluded decisively that contribution of the formate pathway was minimal to the reaction mechanism. Based on these observations presented, the application of redox mechanism has been investigated in this study for WGS over CZPt.

3.2. Redox mechanism

An Eley-Rideal framework for WGS should contain an adsorption step for either CO or H_2O on active sites. Depending on whether CO or H_2O has been adsorbed, there are two possible surface reactions,

$$CO* + H_2O \rightarrow CO_2* + H_2 \quad (12)$$

$$H_2O* + CO \rightarrow CO_2 + H_2* \quad (13)$$

These reactions are followed by desorption of surface bound product. However, an Eley-Rideal framework is seldom considered for WGS over metal/ceria catalyst.

In Langmuir-Hinshelwood framework for WGS, the possibilities for adsorption of reactants CO and H_2O are three fold: both CO and H_2O can adsorb on Pt sites only (single site pathway involving metallic site), both CO and H_2O can adsorb on ceria sites only (single site pathway involving vacancies) or one adsorbs on Pt sites while the other on ceria sites (dual site pathway). In the dual site pathway, Pt sites and the Pt-ceria interface play an important role in affecting surface reactions [23,31,32]. In reaction pathway involving dual sites, the adsorption step is followed by a sequence of surface reactions involving formation of intermediates such as formates, carboxyls which then react to give product surface species. The surface bound product species formed from surface intermediates, then undergo either molecular or associative desorption to release CO_2 and H_2 completing the catalytic cycle.

Catalyst activity studies for WGS conducted over Pt/ceria show that there is a remarkable increase in catalytic activity on addition of ceria as compared to the pure metal surfaces. FTIR studies indicate that CO mainly adsorbs on Pt sites while the ceria sites help in adsorption and activation of H_2O suggesting that both Pt and ceria sites playing important role in the mechanism of WGS [39,40]. Recent DFT based studies indicate that the Pt-ceria interface is the most active region of the catalytic surface [31,32]. Based on the above presented implications, a mechanism that involves active sites on both Pt and ceria, the dual site mechanism based on Langmuir-Hinshelwood framework has been chosen in this study over alternative single site mechanisms.

The microkinetic model consisting the set of 7-reversible elementary steps that have been considered for the redox mechanism along with the corresponding Arrhenius parameters are enlisted in Table 1.

3.3. Selection criteria and literature pertaining to the kinetic parameters for the elementary steps of WGS

3.3.1. $CO + * \Leftrightarrow CO*$

There are two possibilities for the adsorption of CO *i.e.* adsorption on Pt sites and adsorption on ceria sites. However, it is generally accepted in literature that CO adsorption is more favorable on Pt sites. This is predominantly seen in DRIFTS studies which indicate

Table 1
Microkinetic model for redox mechanism of WGS.

Reac/tion	A_i	A_{-i}	E_i (kJ/mol)	E_{-i} (kJ/mol)
1. $CO_{(g)} + *_{(Pt)} \Leftrightarrow CO*_{(Pt)}$	1.5×10^6 atm^{-1}s^{-1}	2×10^{16} s^{-1}	0	133.9
2. $H_2O_{(g)} + (v) \Leftrightarrow H_2O_{(v)}$	10^6 atm^{-1}s^{-1}	10^{13} s^{-1}	0	48.2
3. $H_2O_{(v)} + *_{(Pt)} \Leftrightarrow OH_{(v)} + H*_{(Pt)}$	10^{11} s^{-1}	10^{11} s^{-1}	33.4	45.8
4. $OH_{(v)} + *_{(Pt)} \Leftrightarrow O_{(v)} + H*_{(Pt)}$	10^{12} s^{-1}	10^{11} s^{-1}	107.1	45.7
5. $CO*_{(Pt)} + O_{(v)} \Leftrightarrow CO_2*_{(Pt)} + (v)$	6×10^{10} s^{-1}	1×10^{11} s^{-1}	81.1	100.7
6. $CO_2*_{(Pt)} \Leftrightarrow CO_{2\,(g)} + *_{(Pt)}$	4×10^{12} s^{-1}	10^6 atm^{-1} s^{-1}	15.1	0
7. $2H*_{(Pt)} \Leftrightarrow H_{2(g)} + 2*_{(Pt)}$	6×10^{12} s^{-1}	10^6 atm^{-1} s^{-1}	93.1	0

strong IR absorption around 2099 cm^{-1} characteristic of Pt-CO surface intermediate for ionic platinum [10,41]. This is also indicative in the DFT studies indicating adsorption energy of 133.9 kJ/mol for ionic platinum site compared to the oxygen vacancies [41].

UBI-QEP based calculations of CO adsorption on Pt (111) surface predict a Pt-CO binding energy of 133.9 kJ/mol [42]. Aranifard et al. in their DFT based study of WGS over Pt/ceria report CO adsorption energies to be exothermic, ranging between 1.12–1.77 eV [31,32]. Koop and Duestchmann [43] in their microkinetic model have reported the adsorption energy of 136.1 kJ/mol for CO adsorption on clean Pt site. The adsorption of CO on oxygen vacant site has been reported to be endothermic in nature with adsorption energy of 1.90 eV. These values compare well with the experimentally observed value of 138 kJ/mol for CO adsorption over Pt(111) surface[44]. In accordance with above presented observations, CO adsorption energy of 133.9 kJ/mol was chosen uniformly for all reaction conditions investigated in this study.

3.3.2. $H_2O + v \Leftrightarrow H_2O\ (v)$

H_2O can either adsorb on Pt or ceria active sites. However, it has been widely proposed that the oxide support plays a pivotal role in aiding adsorption and dissociation of water [45–48].

Ceria is generally known for its oxygen storage capacity with the formation of non-stoichiometric reducible states [49]. In addition, Pt and Zn exist in ionic state in CZPt which further promote vacancy formation. These vacancy sites have high affinity for water, as evidenced by various studies from literature. DFT calculations also indicate that the presence of vacancies on the reduced $CeO_{2-x}(111)$ surface aids in both adsorption and dissociation of water. [46–48]. The adsorption energy of H_2O on surface vacancy is in the vicinity range of 0.5–0.6 eV [46–48,50–52]. This is in good agreement with the experimentally measured value of 0.53 eV from temperature programmed desorption (TPD) experiments [53]. Therefore, a H_2O binding energy of 48.2 kJ/mol has been used in the microkinetic model.

3.3.3. $H_2O(v) + {}^* \Leftrightarrow OH(v) + H^*$

To transfer H from the surface hydroxyl species to Pt sites, strong O—H bonds need to be broken. In their *in situ* DRIFTS-SSITKA-MS studies, Kalamaras et al. conclude that O—H bond breaking is most likely the rate determining step in their proposed redox mechanism [27]. In fact, this phenomenon of hydrogen spillover has been theoretically proposed from DFT studies [54]. The activation energy for forward reaction has been proposed to be 33.4 kJ/mol (0.35 eV) and activation energy for backward reaction to be 45.8 kJ/mol [33]. In another DFT study for Pt/ceria, Aranifard et al. estimate activation barriers of 0.32 eV and 0.25 eV for this step considering two different pathways [31,32]. Considering the above presented observations in the present microkinetic model we have considered E_3 = 33.4 kJ/mol and E_{-3} = 45.8 kJ/mol in this study.

3.3.4. $OH(v) + {}^* \Leftrightarrow O(v) + H^*$

As mentioned in the previous Section 3.3.3, it is energetically favorable for hydrogen from H_2O to transfer to Pt sites before desorption. It is also essential to generate O adatoms to facilitate oxidation of CO to give CO_2. With, these two factors in mind, step 3.3.4 was proposed. Spillover of H from Pt to ceria surfaces has been proposed to explain the observed ability of Pt to catalyze the surface reduction of ceria [54].The process involved here is a reverse-spillover. In their DFT study, Aranifard et al. [32], predict adsorbed CO and H species assisted pathway to be in qualitative agreement with the experimental trend. In line with the above propositions, the activation energy values are taken to be 107.1 kJ/mol for E_4 and E_{-4} to be 45.7 kJ/mol

3.3.5. $CO^* + O(v) \Leftrightarrow CO_2{}^* + v$

The oxidation of adsorbed CO by oxygen from ceria to give CO_2 has been widely proposed as one of the fundamental processes that forms the backbone of a redox mechanism [27,34,35]. This surface reaction is RDS for the dual site mechanism proposed for CO oxidation [20]. The energetics and kinetic parameters for this surface reaction are obtained from the apparent activation energy obtained from CO oxidation. The activation energy for forward reaction is taken as 81.1 kJ/mol and the backward reaction energy is taken to be 100.7 kJ/mol.

3.3.6. $CO_2{}^* \Leftrightarrow CO_2 + {}^*$

Deutschmann et al. report CO_2 binding energy of 20.5 kJ/mol on Pt surface [43]. This is in good agreement to the experimentally measured value of (16.02 ± 7.99 kJ/mol) for CO_2 desorption on Pt(111) obtained from single crystal adsorption calorimetry experiments [55]. According to above considerations we have considered CO_2 desorption from Pt sites rather than from ceria sites, and have taken binding energy to be 15.1 kJ/mol across all conditions investigated.

3.3.7. $2H^* \Leftrightarrow H_2 + 2^*$

Microkinetic studies report H_2 desorption energies of 93.1 kJ/mol from clean Pt surface [14,56]. DFT calculations also indicate similar values of 0.99 eV for H_2 dissociative adsorption on Pt(111) surface [57]. This value of 93.1 kJ/mol is also in good agreement with the calorimetric studies for H_2 adsorption energies on Pt surface reported in range from 87.9–103.4 kJ/mol [58]. In line with above presented observations, we have taken 93.1 kJ/mol as the H_2 desorption energy for the microkinetic model.

3.3.8. Pre-exponential values

According to transition state theory (TST), 10^{11}–10^{13} s^{-1} are the pre-exponential factor values proposed for desorption reactions and surface reactions [59]. However, higher pre −exponential factors have been reported for CO desorption [56,60] accordingly, and we have considered 2×10^{16} s^{-1} for CO desorption reaction. For molecular and dissociative adsorption involving immobile transition state, TST predicts a pre-exponential of 10^1 Pa^{-1} s^{-1} ($\sim 10^6$ atm^{-1} s^{-1}). In accordance with this study, the pre exponential values for CO adsorption are considered to be 1.5×10^6 atm^{-1} s^{-1} [13]. The pre-exponential values of dissociative O_2 adsorption and H_2O adsorption are considered to be 4.1×10^6 atm^{-1} s^{-1} [61] and 1.0×10^6 atm^{-1} s^{-1} respectively. The pre-exponential values of CO_2 and H_2 adsorption are considered to be 1.0×10^6 atm^{-1} s^{-1} [13].

3.4. Microkinetic model for CO oxidation

The microkinetic model for CO oxidation is presented in Table 2. The kinetic parameters associated with reversible CO adsorption, surface reaction and reversible CO_2 desorption are taken in accordance with the kinetic parameters presented for WGS. However, the adsorption energy of 100 kJ/mol and desorption pre-exponential of 1.34×10^4 s^{-1} for O_2 are taken in accordance with our previous study [20].

3.5. Calculation of theoretical surface vacancies and platinum site density

As discussed in our previous study [20], theoretical surface vacancy sites and site density of platinum are significant kinetic parameters. In line with the argument presented in our previous study, the theoretical surface vacancy sites can be estimated from

Table 2
Microkinetic model for redox mechanism of CO oxidation.

Reaction	A_i	A_{-i}	E_i (kJ/mol)	E_{-i} (kJ/mol)
1. $CO_{(g)} + *_{(Pt)} \Leftrightarrow CO^*_{(Pt)}$	1.5×10^6 atm^{-1}s^{-1}	2×10^{16} s^{-1}	0	133.9
2. $O_2 + 2(v) \Leftrightarrow 2O_{(v)}$	4.1×10^6 atm^{-1}s^{-1}	1.35×10^4 s^{-1}	0	100.0
3. $CO^*_{(Pt)} + O_{(v)} \Leftrightarrow CO_2{}^*_{(Pt)} + (v)$	6×10^{10} s^{-1}	10^{11} s^{-1}	81.1	100.7
4. $CO_2{}^*_{(Pt)} \Leftrightarrow CO_{2(g)} + *_{(Pt)}$	4×10^{12} s^{-1}	10^6 atm^{-1} s^{-1}	15.1	0

the lattice parameters for cubic catalysts.

$$\text{Surface vacant sites of CePt} = \frac{2}{\sqrt{3}\left(a_0^2\right)} = \frac{2}{\sqrt{3}\left(0.5412 \times 10^{-9}\right)^2}$$

$$= 0.6545 \times 10^{-5}\text{mol/m}^2$$

$$\text{Surface vacant sites of CZPt} = \frac{2}{\sqrt{3}\left(a_0^2\right)} = \frac{2}{\sqrt{3}\left(0.5403 \times 10^{-9}\right)^2}$$

$$= 0.6567 \times 10^{-5}\text{mol/m}^2$$

Where (a_0) is the lattice parameter of the catalyst. Therefore, the site density of surface vacancies and site density of platinum of $Ce_{0.93}Zn_{0.05}Pt_{0.02}O_{2-\delta}$ are taken to be 6.5 μmol/m^2 and 0.263 μmol/m^2 respectively. The theoretical OSC obtained for (111) phase of ceria is in good accordance with the propositions of Madier et al. [62].

3.6. Development of rate expression for dual site CO oxidation and WGS mechanism

In order to develop an implicit rate expression for the microkinetic models presented in Tables 1 and 2 and to facilitate the application of the kinetic parameters, reaction route analysis has been used. The terminology and the prospectus of the RR analysis can be found elsewhere [15].

Briefly, the methodology employs the Langmuir-Hinshelwood-Hougen-Watson approach to estimate the individual step resistances. Individual step resistance is the inverse of the forward rate of the individual elementary reaction calculated under the assumption that elementary step under consideration is rate determining and rest of the elementary steps in the mechanism are in partial equilibrium. A detailed explanation and derivation for the development of expressions for individual step resistances for CO oxidation can be found elsewhere [20].

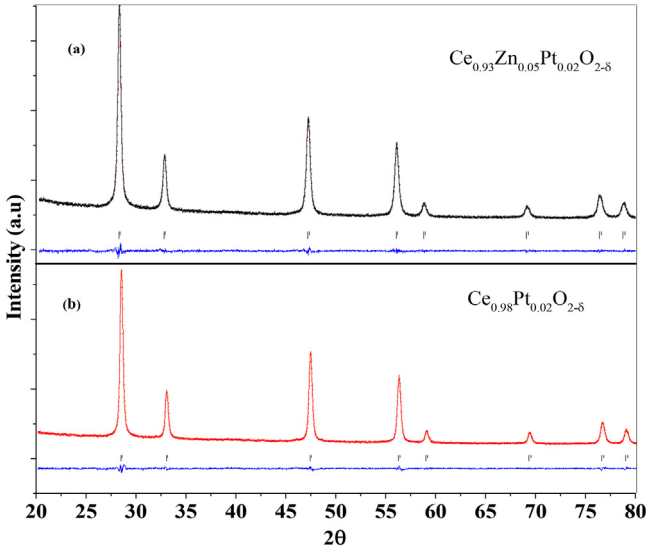

Fig. 1. Refined XRD pattern of (a) CZPt and (b) CePt.

Eqs. (14)–(20) present the analytic expressions for individual step resistances in microkinetic model presented for WGS in Table 1.

$$R_1^w = \frac{\left(1 + \sqrt{\frac{P_{H_2}}{K_7}} + \frac{P_{CO_2}}{K_6} + \frac{P_{CO_2}P_{H_2}}{K_2K_3K_4K_5K_6K_7P_{H_2O}}\right)}{k_1P_{CO}} \tag{14}$$

$$R_2^w = \frac{\left(1 + \sqrt{\frac{P_{H_2}}{K_7}} \cdot \frac{P_{CO_2}}{K_1K_4K_5K_6P_{CO}} + \frac{P_{CO_2}}{K_1K_5K_6P_{CO}} + \frac{P_{CO_2}P_{H_2}}{K_1K_3K_4K_5K_6K_7P_{CO}}\right)}{k_2P_{H_2O}} \tag{15}$$

$$R_3^w = \frac{\left(1 + K_2P_{H_2O} + \frac{P_{CO_2}}{K_1K_4K_5K_6P_{CO}}\sqrt{\frac{P_{H_2}}{K_7}} + \frac{P_{CO_2}}{K_1K_5K_6P_{CO}}\right)\left(1 + K_1P_{CO} + \frac{P_{CO_2}}{K_6} + \sqrt{\frac{P_{H_2}}{K_7}}\right)}{k_3K_2P_{H_2O}} \tag{16}$$

$$R_4^w = \frac{\left(1 + K_2P_{H_2O} + K_2K_3P_{H_2O}\sqrt{\frac{K_7}{P_{H_2}}} + \frac{P_{CO_2}}{K_1K_5K_6P_{CO}}\right)\left(1 + K_1P_{CO} + \frac{P_{CO_2}}{K_6} + \sqrt{\frac{P_{H_2}}{K_7}}\right)}{k_4K_2K_3\sqrt{\frac{K_7}{P_{H_2}}}P_{H_2O}} \tag{17}$$

$$R_5^w = \frac{\left(1 + K_2P_{H_2O} + K_2K_3P_{H_2O}\sqrt{\frac{K_7}{P_{H_2}}} + \frac{K_2K_3K_4K_7P_{H_2O}}{P_{H_2}}\right)\left(1 + K_1P_{CO} + \frac{P_{CO_2}}{K_6} + \sqrt{\frac{P_{H_2}}{K_7}}\right)}{k_5\frac{K_1K_2K_3K_4K_7P_{H_2O}P_{CO}}{P_{H_2}}} \tag{18}$$

$$R_6^w = \frac{\left(1 + K_1P_{CO} + \frac{K_1K_2K_3K_4K_5K_7P_{CO}P_{H_2O}}{P_{H_2}} + \sqrt{\frac{P_{H_2}}{K_7}}\right)}{k_6\frac{K_1K_2K_3K_4K_5K_7P_{CO}P_{H_2O}}{P_{H_2}}} \tag{19}$$

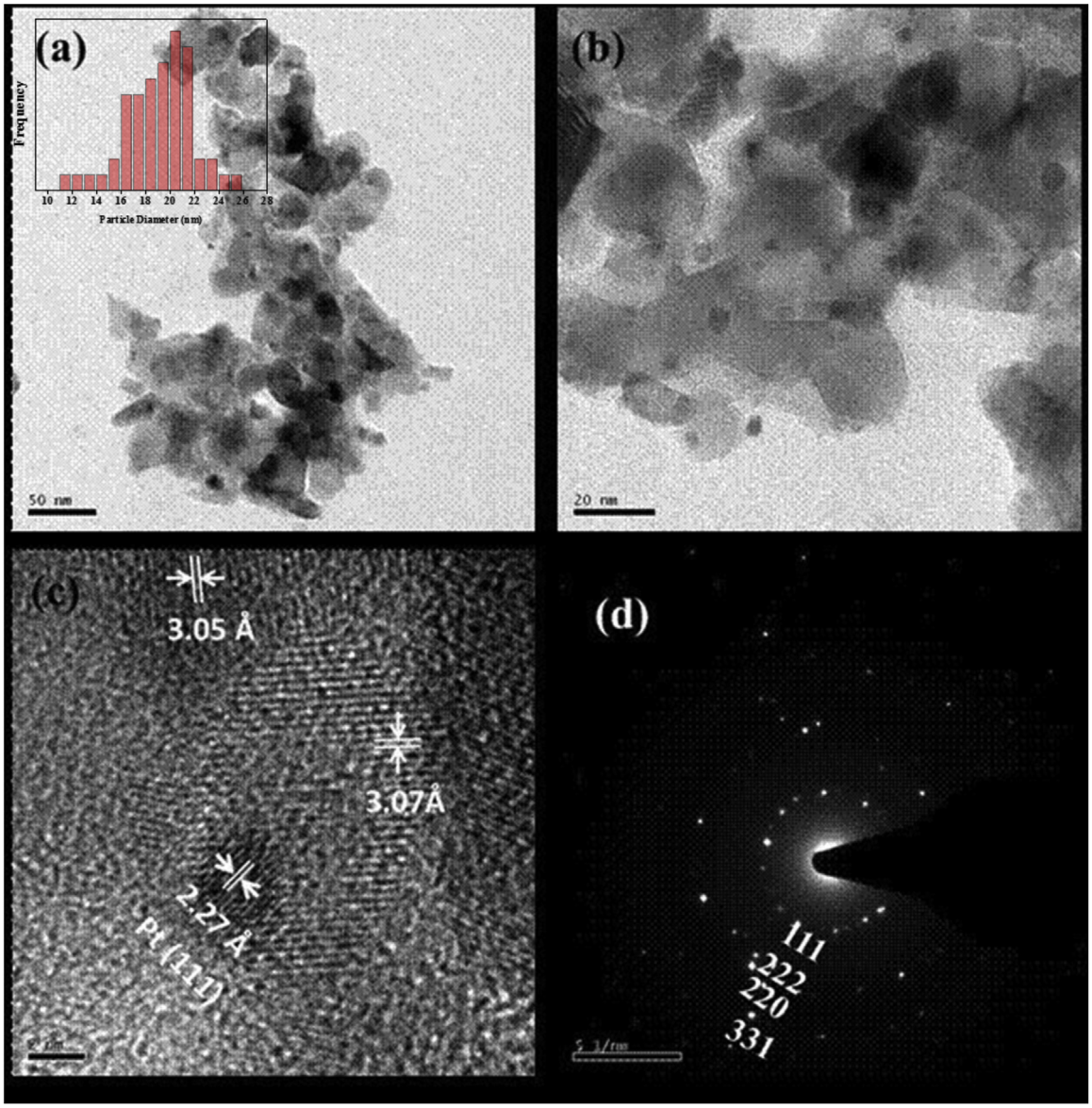

Fig. 2. (a), (b) Bright-field TEM image of zinc and platinum co-doped ceria (Inset particle size distribution) (c) HRTEM image of Zinc and Platinum co-doped ceria (d) SAED pattern for zinc and platinum co-doped ceria.

$$R_7^w = \frac{\left(1 + K_1 P_{CO} + \frac{P_{CO_2}}{K_6} + \sqrt{\frac{K_1 K_2 K_3 K_4 K_5 K_6 P_{CO} P_{H_2O}}{P_{CO_2}}}\right)^2}{k_7 \frac{K_1 K_2 K_3 K_4 K_5 K_6 P_{CO} P_{H_2O}}{P_{CO_2}}} \quad (20)$$

In Eqs. (14)–(20), P_{CO}, P_{H_2O}, P_{CO_2}, P_{H_2} represent the partial pressures of CO, H_2O CO_2, and H_2 respectively. K_i represents the equilibrium constant of the individual reversible elementary reaction. The individual rate constant k_i of ith surface reaction is given by the Eq. (21),

$$k_i = A_i \times \sigma \times e^{-\frac{E_i}{RT}} \quad (21)$$

In Eq. (21), A_i, is the pre-exponential factor, σ is the site density and E_i is the activation energy of the i^{th} surface reaction. For surface reaction taking place on surface vacancies, surface vacancy site density has been used and for the reactions taking place on metallic site, ionic Pt site density has been used.

4. Results and discussion

The X-ray diffraction (XRD) pattern represented in Fig. 1 showed no significant peaks for metallic platinum, metallic zinc and zinc oxide. The refined XRD pattern confirmed the fluorite structure, Fm-3 m space group (no. 225) of ceria. The refined XRD pattern also showed a decrease in lattice parameter of 5.403 Å for CZPt compared to 5.411 Å and 5.409 Å for pure ceria and platinum doped ceria respectively. This lattice parameter for zinc and platinum doped ceria is consistent with lattice parameter for zinc doped ceria [16]. The crystalline sizes of CZPt and CePt were calculated to be 23 ± 1 nm using the Scherrer formula. The bright-field images displayed in Fig. 2(a), (b), show relatively lower presence of platinum metallic particles. This can also be inferred from the HRTEM micrographs portraying the presence of platinum nanoparticles showing (111) planes with d-spacing of 2.27 Å in Fig. 2(c). The micrographs also shows the presence of (111) plane of CeO_2 with d-spacing of 3.1 Å [8]. Fig. 2(d) presents the selected area electron diffraction (SAED) pattern of CZPt obtained from TEM. As observed from the d-spacing values obtained from the diffraction pattern, the peaks

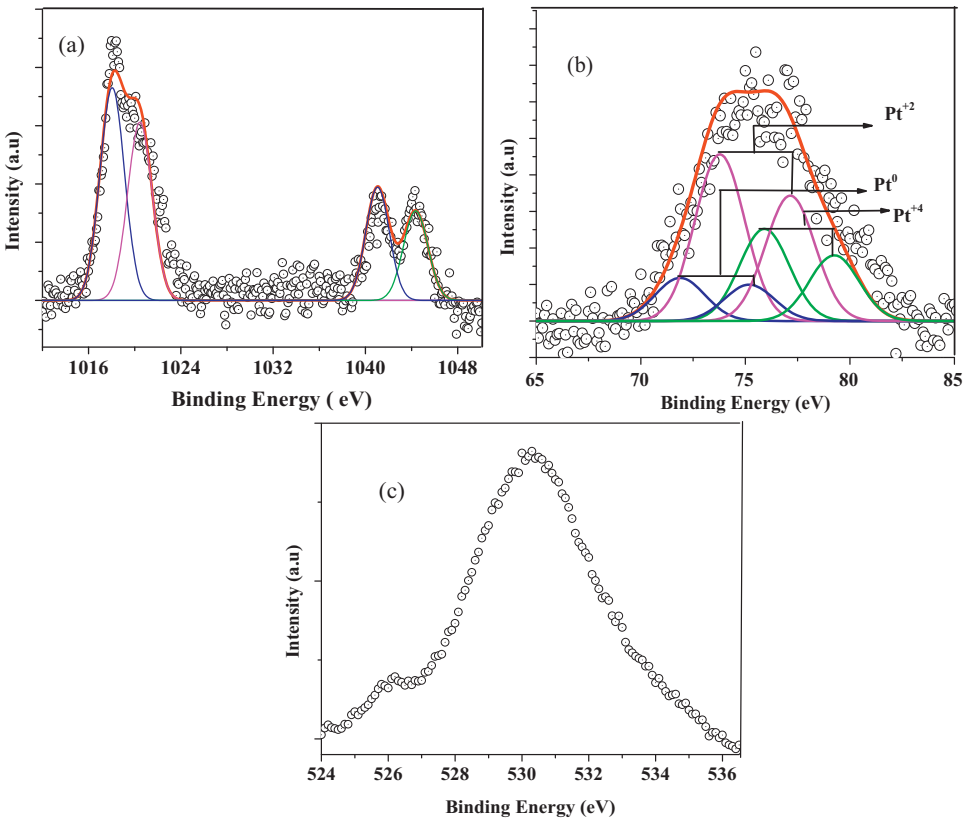

Fig. 3. (a). De-convoluted XPS spectra of (a) Zn 2p (b) Pt 4f and (c) O1s spectra of CZPt.

were identified as 111, 220, 222, 331 planes corresponding to ceria. Similar to the XRD pattern no peaks for metallic platinum and zinc patterns were seen in SAED pattern. The average particle size was calculated to be 19.6 ± 2.4 nm from TEM micrographs.

Fig. 3(a)–(c) presents, the XPS of different elements present in the catalysts. The relative XPS signals were corrected based on reference C1 s adventious carbon peak of 284.8 eV which has been used as internal standard for correcting the peak signals. The catalyst exhibited adventious carbon peak at C1s 285.2 eV, a correction factor accordingly was employed for the spectra of all the elements. Fityk® software has been used to deconvolute and the XPS spectra of the all the elements were deconvoluted using Gaussian functions. The background of the Pt_{4f} spectra was corrected using linear correction and the resultant spectra was de-convoluted into three distinctive peaks resolved for Pt 4f $_{5/2}$ and Pt 4f $_{7/2}$ spin orbitals respectively. The peaks at 71.9 eV and 75.3 eV for Pt 4f $_{5/2}$ and Pt 4f $_{7/2}$ spin orbitals represent the metallic state of Pt. Similarly, peaks at 73.85 eV, 77.19 eV and 75.8, 79.14 eV for Pt 4f $_{5/2}$ and Pt 4f $_{7/2}$ spin orbitals represent the +2 and +4 oxidation state of Pt respectively [63]. The percentages of oxidation states of platinum were calculated using deconvoluted peak intensities and were found to be 16.8%, 61.6%, 21.6% for Pt^0, Pt^{+2} and Pt^{+4} respectively. As observed from the deconvoluted Pt XPS spectra, Pt is substituted mostly in +2 state, thus confirming the ionic substitution of Pt in ceria This can also be inferred from the change in the d-spacing values obtained from HRTEM. The background of the XPS spectra for Zn 2p was corrected using Shirley correction method and the resultant spectra was de-convoluted into two distinctive peaks pertaining to the Zn^{+2} states having binding energies of 1017.9, 1020.6 eV for $2p_{1/2}$ and 1041.2, 1044 eV for $2p_{3/2}$ respectively. This result is in good agreement with the Zn 2p XPS studies pertaining to different substituted zinc catalysts [64,65]. The O1s XPS shows most intense peak at 530.1 eV confirming the presence of oxygen as lattice oxygen in the corresponding metal oxide [66].

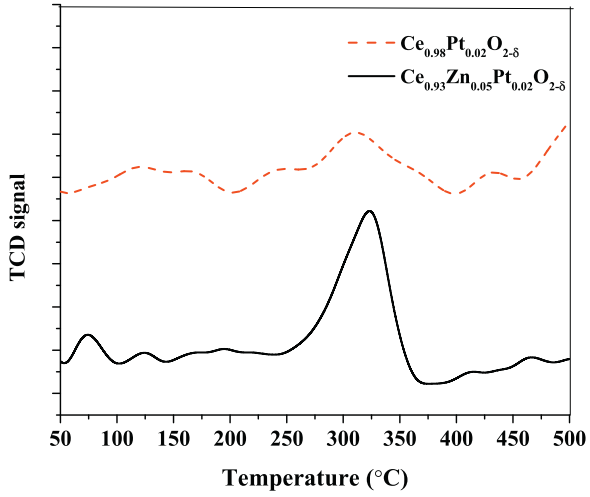

Fig. 4. H_2-TPR profile of (a) CZPt and (b) CePt.

Fig. 4 shows the H_2-TPR study of the catalysts. As seen from the figure, the OSC of $Ce_{0.93}Zn_{0.05}Pt_{0.02}O_{2-\delta}$ is significant in the operational temperature range (250–320 °C) for WGS thus asserting the usage of the catalyst for single stage WGS conditions. The H_2 uptake measured till 400 °C was found to be 1507 μmol/g for CZPt and 1037 μmol/g for CePt respectively. The BET surface area of the CZPt was found to be 14 m^2/g.

4.1. Catalytic activity

Differential flow reactor approximations are predominantly used to understand and quantify the catalytic activity [20]. The experimental rates at different temperatures are obtained by plot-

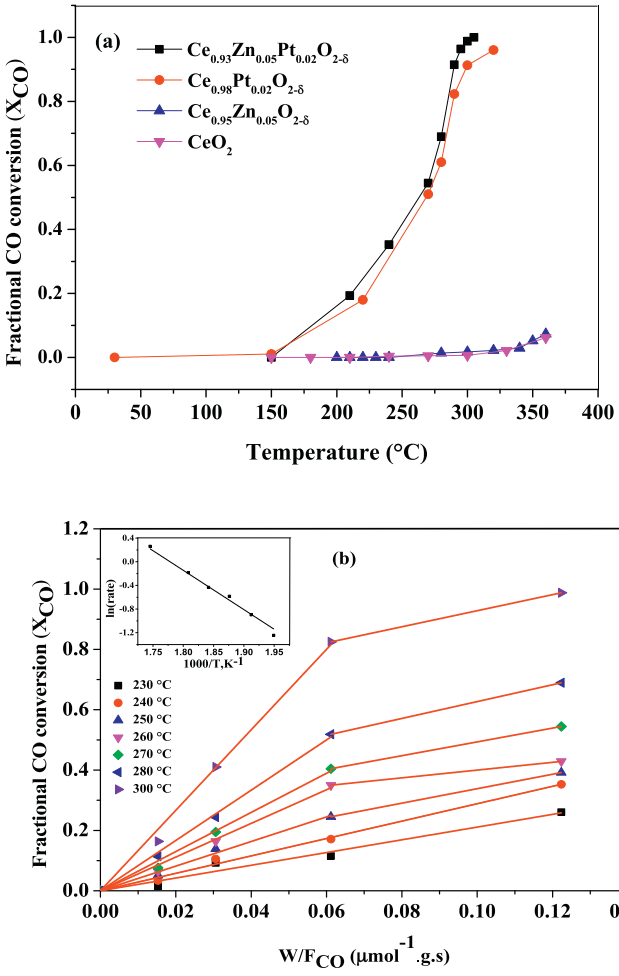

Fig. 5. (a). Comparison of catalytic performance for WGS pertaining to (a) CZPt with CePt (b) Differential reactor approximation and Arrhenius plot of intrinsic rate (inset).

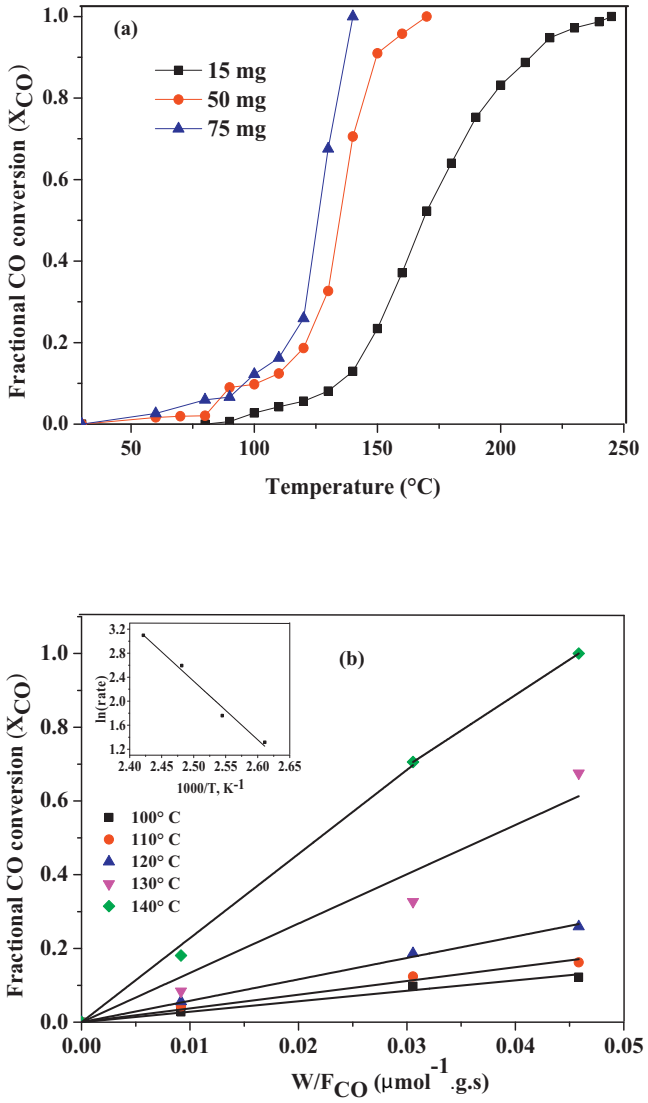

Fig. 6. (a). Catalytic performance pertaining to CZPt for CO oxidation. (b) Differential reactor approximation and Arrhenius plot of intrinsic rate (inset).

ting the ratio of weight of catalyst to molar flow rate of limiting reactant CO (W/F_{CO}) with the fractional CO conversion at different experimental temperatures. Similar approach has been employed in this study to estimate the intrinsic reaction rates and apparent activation energy of WGS and CO oxidation reactions respectively.

Figs. 5(a) and 6(a) present the activity of the catalysts portraying the fractional CO conversion against the experimental temperature range. In order to differentiate the hierarchy of zinc and platinum co-doping in ceria for WGS activity, the fractional CO conversion using mono metal doping of zinc and platinum in ceria has been tested. From Fig. 5(a), it can be seen that as compared to other catalysts zinc and platinum co doped ceria has higher catalytic activity for WGS. Figs. 5(b) and 6(b) show the linear variation of fractional conversions of CO with W/F_{CO} for CO oxidation and WGS respectively. From the figures, it can be seen that the differential reactor proximity, *i.e.*, the extent of linearity is seen till 30% CO conversion for WGS reaction and 80% CO conversion for CO oxidation. Figs. 5(b) and 6(b) show the Arrhenius plot of intrinsic rates against temperature for WGS and CO oxidation. As mentioned earlier, the hierarchy of zinc and platinum doped ceria is also evident from the activation energy as compared to other catalysts. The apparent activation energy obtained for WGS in this study for CZPt is 55 kJ/mol akin to 63 kJ/mol for CePt [4]. The activation energy for CO oxidation for CZPt is found to be 81.1 kJ/mol. Tables 3a and 3b present the comparison of the activation energy obtained in this study to the apparent activation energies reported in the literature. The reac-

Table 3a
Comparison of activation energies for CO oxidation.

Catalyst	Activation Energy (kJ/mol)	Reference
$Ce_{0.83}Sn0._{15}Pd_{0.02}O_{2-\delta}$	83.6	[69]
$Ce_{0.98}Pd_{0.02}O_{2-\delta}$	121.0	[70]
$Ce_{0.95}Ru_{0.05}O_{1.97}$	92.2	[71]
$Ce_{0.93}Zn_{0.05}Pt_{0.02}O_{2-\delta}$	81.1	(This work)

Table 3b
Comparison of activation energies for WGS.

Catalyst	Activation Energy (kJ/mol)	Reference
$Ce_{0.98}Pt_{0.02}O_{2-\delta}$	62.3	[4]
$Ti_{0.84}Pt_{0.01}Fe_{0.15}O_{2-\delta}$	63.0	[7]
$Ce_{0.78}Ti_{0.2}Pt_{0.02}O_{2-\delta}$	56.5	[4]
$Ce_{0.85}Fe_{0.1}Ru_{0.05}O_{2-\delta}$	56.0	[72]
0.5 wt% Pt/Ce-Y	85.0	[10]
0.5 wt% Pt/Ce-Gb	85.0	[10]
0.5 wt% Pt/Ce-Zn	83.6	[10]
0.5 wt% Pt/Ce-Mg	85.0	[10]
0.5 wt% Pt/Ce-Ca	87.4	[10]
0.5 wt% Pt/Ce-Zr	83.2	[10]
0.5 wt% Pt/Ce-Yb	78.6	[10]
$Ce_{0.93}Zn_{0.05}Pt_{0.02}O_{2-\delta}$	55.0	(This work)
$Ce_{0.88}Al_{0.1}Pt_{0.02}O_{2-\delta}$	51.0	[9]

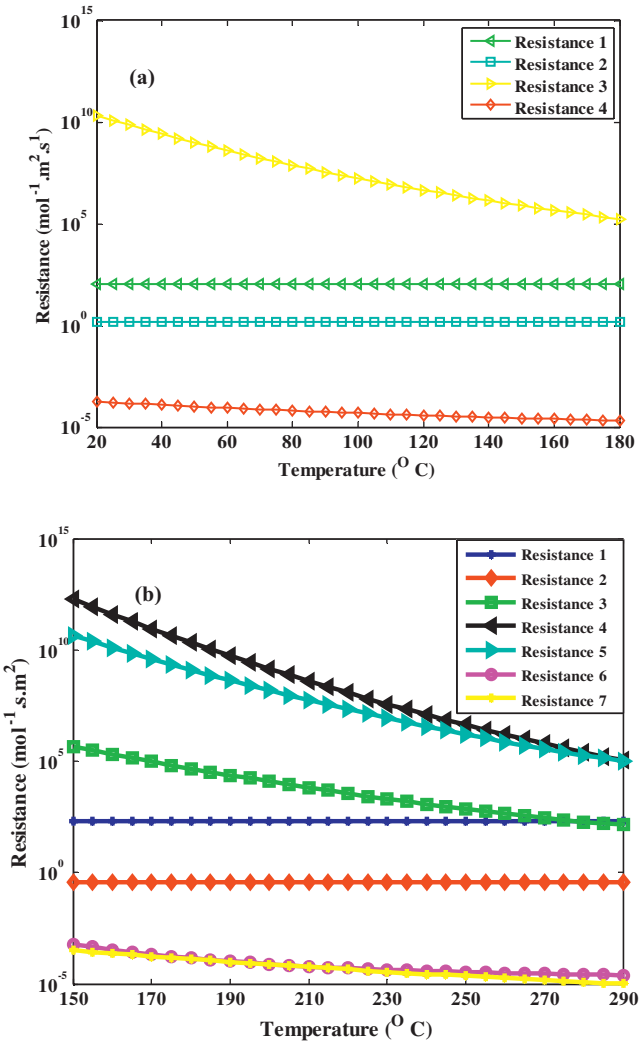

Fig. 7. Step resistance plots against experimental temperature range (a) CO oxidation (b) WGS (symbols represent the experimental data, Solid lines represent the simulation predictions).

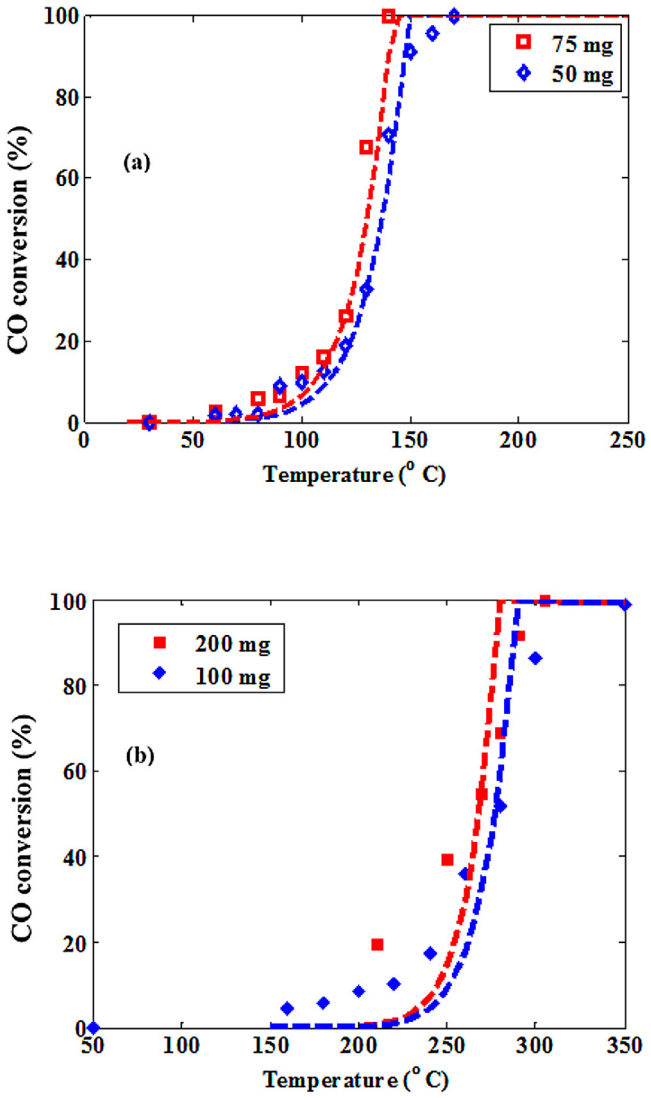

Fig. 8. Isothermal PFR predictions against experimental data. (a) CO oxidation (b) WGS (symbols represent the experimental data, Solid lines represent the simulation predictions).

tion was assumed to proceed in kinetic regime under isothermal conditions devoid of mass transfer and heat transfer limitations. This can be explained based on the mass transfer and heat transfer constraints [67]. The Weisz modulus for inter phase mass transfer is given in Eq. (22 a)

$$\phi = \frac{(n+1)\,R_{obs}\cdot\rho_{cat}\left(d_p/6\right)^2}{2D_{eff}C_s} \tag{22 a}$$

The interphase heat transfer constraint is given in Eq. (22 b)

$$\frac{|\Delta H^0_{rxn}|R_{obs}\rho_{cat}d_pE}{h_fT^2R} \tag{22 b}$$

The values obtained at 300 °C, for Eqs. (22 a) and (22 b) are 0.017 and 1.02×10^{-4} respectively which are within the limitation values of 0.25 and 0.15 for Eqs. (22 a) and (22 b), thus validating the assumption of precedence of reaction in kinetic regime at isothermal conditions.

4.2. Validation of microkinetic model

In order to validate the kinetic parameters proposed in this work, an isothermal PFR model has been considered [20,68]. The design equations of the plug flow reactor (PFR) model are given in Eqs. (23 a) and (23 b).

$$(\rho u)\frac{dy_i}{dz} = \left(\frac{a}{V}\right)M_i\sum_j v_{i,j}R_j \quad \text{for, } i = 1\ldots., N_g \tag{23 a}$$

$$\sum_{i=1}^{N_S}\theta_i = 1 \quad \text{for, } i = 1\ldots, N_s \tag{23 b}$$

The values of individual step resistances plotted using the kinetic parameters presented in Table 2 for CO oxidation are shown in Fig. 7(a). As seen from the figure, Resistance 3, which denotes the formation for surface CO_2 species is found to be RDS and is in good agreement with our previous study [20]. Therefore, the rate expression for CO oxidation would be given as shown in Eq. (24).

$$r_{CO} = \frac{k_3K_1P_{CO}\sqrt{K_2P_{O_2}}}{(1+(K_1P_{CO}))\left(1+\sqrt{K_2P_{O_2}}\right)} \tag{24}$$

Fig. 7(b) shows the variation of step resistances of WGS been plotted against the experimental temperature range. From the resistance plot it can be seen that resistance 4 which denotes the

surface reaction of OH species to give O species and H species offers the maximum resistance, thus is the RDS of the system. This result inferred from the reaction route analysis is in good agreement with RDS proposed by Kalamaras et al. [27]. Based on the above RDS, the rate expression for WGS denoted as r^{w}_{OR} is obtained using reaction route analysis as shown in Eq. (25)

$$r^{w}_{OP}=\frac{k_4K_2K_3\sqrt{\frac{K_7}{P_{H_2}}}P_{H_2O}\left(1-\frac{P_{CO_2}P_{H_2}}{K_4K_2K_3K_7K_1K_5K_6P_{CO}P_{H_2O}}\right)}{\left(1+K_2P_{H_2O}+K_2K_3P_{H_2O}\sqrt{\frac{K_7}{P_{H_2}}}+\frac{P_{CO_2}}{K_1K_5K_6P_{CO}}\right)\left(1+K_1P_{CO}+\frac{P_{CO_2}}{K_6}+\sqrt{\frac{P_{H_2}}{K_7}}\right)} \quad (25)$$

The validity of the kinetic parameters proposed and the rate expressions derived using RR analysis is tested against CO conversion obtained from the experimental data. Fig. 8(a) presents the kinetic parameters and intrinsic rate expressions (Eq. (24)) against the experimental trend for CO oxidation and Fig. 8(b) presents the kinetic parameters and intrinsic rate expressions predictions (Eq. (25)) against the experimental trend for WGS. As seen from the figures, the analytical rate expressions and the kinetic parameters proposed in the microkinetic models predicted the experimental trend to reasonable accuracy thus validating the robustness and applicability of the kinetic modelling procedure developed in this study.

5. Conclusions

This study aims at developing novel single-stage water shift reaction catalysts. Zinc and platinum co-doped ceria catalysts have been synthesized using one-step solution combustion procedure. The catalysts were characterized by XRD, XPS, TEM, BET and H_2-TPR techniques. As shown from the different characterization techniques, platinum and zinc have been co-doped in ionic state into ceria asserting the usage of CZPt for low temperature WGS. The co-doping of ceria with zinc and platinum increased the WGS activity, which can be attributed to the enhancement in the OSC. This was evident from the H_2-TPR studies, with CZPt displaying higher H_2 consumption compared to CePt.

Based on the kinetic parameters obtained from the literature, a comprehensive microkinetic model has been developed for both CO oxidation and WGS. Using the reaction route analysis, an analytical rate expression has been developed for CO oxidation and WGS, based on the RDS. The rate expression and kinetic parameters predicted the experimental trend to reasonable accuracy for different experimental conditions involving different catalyst loading and wider experimental temperature conditions, thus validating the proposed microkinetic model.

Acknowledgements

The authors thank the Department of science and technology (DST), India for the financial support. The authors also acknowledge the characterization facilities for XPS and TEM at CeNSE and AFM Departments at IISc. The corresponding author thanks DST for the J.C. Bose fellowship.

References

[1] R.J. Gorte, Ceria in catalysis: from automotive applications to the water–gas shift reaction, AIChE J. 56 (2010) 1126–1135.
[2] P.A. Deshpande, G. Madras, Support-dependent activity of noble metal substituted oxide catalysts for the water gas shift reaction, AIChE J. 56 (2010) 2662–2676.
[3] V.M. Shinde, G. Madras, Water gas shift reaction over multi-component ceria catalysts, Appl. Catal. B 123 (2012) 367–378.
[4] S. Sharma, P.A. Deshpande, M.S. Hegde, G. Madras, Nondeactivating nanosized ionic catalysts for water-gas shift reaction, Ind. Eng. Chem. Res. 48 (2009) 6535–6543.
[5] P.A. Deshpande, M.S. Hegde, G. Madras, Pd and Pt ions as highly active sites for the water-gas shift reaction over combustion synthesized zirconia and zirconia-modified ceria, Appl. Catal. B 96 (2010) 83–93.
[6] P.A. Deshpande, M.S. Hegde, G. Madras, A mechanistic model for the water-gas shift reaction over noble metal substituted ceria, AIChE J. 56 (2010) 1315–1324.
[7] V.M. Shinde, G. Madras, Low temperature CO oxidation and water gas shift reaction over Pt/Pd substituted in Fe/TiO_2 catalysts, Int. J. Hydrogen Energy 37 (2012) 18798–18814.
[8] V.M. Shinde, G. Madras, Nanostructured Pd modified Ni/CeO_2 catalyst for water gas shift and catalytic hydrogen combustion reaction, Appl. Catal. B 132 (2013) 28–38.
[9] V.M. Shinde, G. Madras, A single-Stage water-gas shift reaction over highly active and stable Si- and Al-substituted Pt/CeO_2 catalysts, ChemCatChem 4 (2012) 1968–1978.
[10] P. Panagiotopoulou, J. Papavasiliou, G. Avgouropoulos, T. Ioannides, D.I. Kondarides, Water-gas shift activity of doped Pt/CeO_2 catalysts, Chem. Eng. J. 134 (2007) 16–22.
[11] O.H. Laguna, F.R. Sarria, M.A. Centeno, J.A. Odriozola, Gold supported on metal-doped ceria catalysts (M = Zr, Zn and Fe) for the preferential oxidation of CO (PROX), J. Catal. 276 (2010) 360–370.
[12] O.H. Laguna, M.A. Centeno, F. Romero-Sarria, J.A. Odriozola, Oxidation of CO over gold supported on Zn-modified ceria catalysts, Catal. Today 172 (2011) 118–123.
[13] C.A. Callaghan, S.A. Vilekar, I. Fishtik, R. Datta, Topological analysis of catalytic reaction networks: water gas shift reaction on Cu (111), Appl. Catal. A 345 (2008) 213–232.
[14] A. Mhadeshwar, D. Vlachos, Microkinetic modeling for water-promoted CO oxidation, water-gas shift, and preferential oxidation of CO on Pt, J. Phys. Chem. B 108 (2004) 15246–15258.
[15] S.A. Vilekar, I. Fishtik, R. Datta, The steady-state kinetics of a catalytic reaction sequence, Chem. Eng. Sci. 64 (2009) 1968–1979.
[16] L.A. Ying, J. Liu, L.Y. Mo, H. Lou, X.M. Zheng, Hydrogen production by oxidative steam reforming of methanol over $Ce_{1-x}Zn_xO_y$ catalysts prepared by combustion method, Int. J. Hydrogen Energy 37 (2012) 1002–1006.
[17] F.J. Lin, R. Delmelle, T. Vinodkumar, B.M. Reddy, A. Wokaun, I. Alxneit, Correlation between the structural characteristics, oxygen storage capacities and catalytic activities of dual-phase Zn-modified ceria nanocrystals, Catal. Sci. Technol. 5 (2015) 3556–3567.
[18] M. Manzoli, G. Avgouropoulos, T. Tabakova, J. Papavasiliou, T. Ioannides, F. Boccuzzi, Preferential CO oxidation in H_2-rich gas mixtures over Au/doped ceria catalysts, Catal. Today 138 (2008) 239–243.
[19] G. Avgouropoulos, M. Manzoli, F. Boccuzzi, T. Tabakova, J. Papavasiliou, T. Ioannides, V. Idakiev, Catalytic performance and characterization of Au/doped-ceria catalysts for the preferential CO oxidation reaction, J. Catal. 256 (2008) 237–247.
[20] R.K. Mandapaka, G. Madras, Microkinetic modeling of CO oxidation on ionic palladium-substituted ceria, Ind. Eng. Chem. Res. 55 (2016) 2309–2318.
[21] J. Thormann, L. Maier, P. Pfeifer, U. Kunz, O. Deutschmann, K. Schubert, Steam reforming of hexadecane over a Rh/CeO_2 catalyst in microchannels: experimental and numerical investigation, Int. J. Hydrogen Energy 34 (2009) 5108–5120.
[22] J. Vecchietti, A. Bonivardi, W. Xu, D. Stacchiola, J.J. Delgado, M. Calatayud, S.E. Collins, Understanding the role of oxygen vacancies in the water gas shift reaction on ceria-supported platinum catalysts, ACS Catal. 4 (2014) 2088–2096.
[23] J.A. Rodriguez, P. Liu, J. Hrbek, J. Evans, M. Pérez, Water gas shift reaction on Cu and Au nanoparticles supported on CeO_2(111) and ZnO(0001): intrinsic activity and importance of support interactions, Angew. Chem. Int. Ed. 46 (2007) 1329–1332.
[24] A.A. Phatak, N. Koryabkina, S. Rai, J.L. Ratts, W. Ruettinger, R.J. Farrauto, G.E. Blau, W.N. Delgass, F.H. Ribeiro, Kinetics of the water-gas shift reaction on Pt catalysts supported on alumina and ceria, Catal. Today 123 (2007) 224–234.
[25] T. Baidya, G. Dutta, M.S. Hegde, U.V. Waghmare, Noble metal ionic catalysts: correlation of increase in CO oxidation activity with increasing effective charge on Pd ion in Pd ion substituted $Ce_{1-x}M_xO_{2-\delta}$(M = Ti, Zr and Hf), Dalton Trans. (2009) 455–464.
[26] W.Q. Xu, R. Si, S.D. Senanayake, J. Llorca, H. Idriss, D. Stacchiola, J.C. Hanson, J.A. Rodriguez, In situ studies of CeO_2-supported Pt, Ru, and Pt-Ru alloy catalysts for the water-gas shift reaction: active phases and reaction intermediates, J. Catal. 291 (2012) 117–126.
[27] C.M. Kalamaras, S. Americanou, A.M. Efstathiou, Redox vs associative formate with –OH group regeneration WGS reaction mechanism on Pt/CeO_2: Effect of platinum particle size, J. Catal. 279 (2011) 287–300.
[28] D. Tibiletti, A. Goguet, D. Reid, F.C. Meunier, R. Burch, On the need to use steady-state or operando techniques to investigate reaction mechanisms: an in situ DRIFTS and SSITKA-based study example, Catal. Today 113 (2006) 94–101.
[29] G. Jacobs, S. Khalid, P.M. Patterson, D.E. Sparks, B.H. Davis, Water-gas shift catalysis: kinetic isotope effect identifies surface formates in rate limiting step for Pt/ceria catalysts, Appl. Catal. A 268 (2004) 255–266.
[30] F.C. Meunier, D. Tibiletti, A. Goguet, D. Reid, R. Burch, On the reactivity of carbonate species on a Pt/CeO_2 catalyst under various reaction atmospheres:

application of the isotopic exchange technique, Appl. Catal. A 289 (2005) 104–112.
[31] S. Aranifard, S.C. Ammal, A. Heyden, On the importance of the associative carboxyl mechanism for the water-gas shift reaction at Pt/CeO_2 interface sites, J. Phys. Chem. C 118 (2014) 6314–6323.
[32] S. Aranifard, S.C. Ammal, A. Heyden, On the importance of metal-oxide interface sites for the water-gas shift reaction over Pt/CeO_2 catalysts, J. Catal. 309 (2014) 314–324.
[33] R.T. Kinch, C.R. Cabrera, Y. Ishikawa, A density-functional theory study of the water-gas shift mechanism on Pt/ceria(111), J. Phys. Chem. C 113 (2009) 9239–9250.
[34] R.J. Gorte, S. Zhao, Studies of the water-gas-shift reaction with ceria-supported precious metals, Catal. Today 104 (2005) 18–24.
[35] Y. Li, Q. Fu, M. Flytzani-Stephanopoulos, Low-temperature water-gas shift reaction over Cu- and Ni-loaded cerium oxide catalysts, Appl. Catal. B 27 (2000) 179–191.
[36] A. Goguet, F.C. Meunier, D. Tibiletti, J.P. Breen, R. Burch, Spectrokinetic investigation of reverse water-gas-shift reaction intermediates over a Pt/CeO_2 catalyst, J. Phys. Chem. B 108 (2004) 20240–20246.
[37] F.C. Meunier, A. Goguet, C. Hardacre, R. Burch, D. Thompsett, Quantitative DRIFTS investigation of possible reaction mechanisms for the water-gas shift reaction on high-activity Pt- and Au-based catalysts, J. Catal. 252 (2007) 18–22.
[38] R. Burch, A. Goguet, F.C. Meunier, A critical analysis of the experimental evidence for and against a formate mechanism for high activity water-gas shift catalysts, Appl. Catal. A 409 (2011) 3–12.
[39] G. Jacobs, B.H. Davis, Low temperature water-gas shift: applications of a modified SSITKA-DRIFTS method under conditions of H_2 co-feeding over metal/ceria and related oxides, Appl. Catal. A 333 (2007) 192–201.
[40] K.G. Azzam, I.V. Babich, K. Seshan, L. Lefferts, Bifunctional catalysts for single-stage water-gas shift reaction in fuel cell applications. Part 1. Effect of the support on the reaction sequence, J. Catal. 251 (2007) 153–162.
[41] G. Dutta, A. Gupta, U.V. Waghmare, M.S. Hegde, CO adsorption on ionic Pt, Pd and Cu sites in $Ce_{1-x}M_xO_{2-\delta}$ (M = Pt2+, Pd2+, Cu2+), J. Chem. Sci. 123 (2011) 509–516.
[42] M.J. Hei, H.B. Chen, J. Yi, Y.J. Lin, Y.Z. Lin, G. Wei, D.W. Liao, CO_2-reforming of methane on transition metal surfaces, Surf. Sci. 417 (1998) 82–96.
[43] J. Koop, O. Deutschmann, Detailed surface reaction mechanism for Pt-catalyzed abatement of automotive exhaust gases, Appl. Catal. B 91 (2009) 47–58.
[44] T. Engel, G. Ertl, Elementary steps in the catalytic oxidation of carbon monoxide on platinum metals, Adv. Catal. 28 (1979) 1–78.
[45] K.G. Azzam, I.V. Babich, K. Seshan, L. Lefferts, A bifunctional catalyst for the single-stage water-gas shift reaction in fuel cell applications. Part 2. Roles of the support and promoter on catalyst activity and stability, J. Catal. 251 (2007) 163–171.
[46] H.A. Hansen, C. Wolverton, Kinetics and thermodynamics of H_2O dissociation on reduced CeO_2(111), J. Phys. Chem. C 118 (2014) 27402–27414.
[47] B. Chen, Y. Ma, L. Ding, L. Xu, Z. Wu, Q. Yuan, W. Huang, Reactivity of hydroxyls and water on a CeO_2 (111) thin film surface: the role of oxygen vacancy, J. Phys. Chem. C 117 (2013) 5800–5810.
[48] D.R. Mullins, P.M. Albrecht, T.-L. Chen, F.C. Calaza, M.D. Biegalski, H.M. Christen, S.H. Overbury, Water dissociation on CeO_2 (100) and CeO_2 (111) thin films, J. Phys. Chem. C 116 (2012) 19419–19428.
[49] A. Trovarelli, Catalysis by Ceria and Related Materials, World Scientific, London, 2002.
[50] M.A. Henderson, The interaction of water with solid surfaces: fundamental aspects revisited, Surf. Sci. Rep. 46 (2002) 1–308.
[51] A. Goguet, R. Burch, Y. Chen, C. Hardacre, P. Hu, R.W. Joyner, F.C. Meunier, B.S. Mun, A. Thompsett, D. Tibiletti, Deactivation mechanism of a Au/$CeZrO_4$ catalyst during a low-temperature water gas shift reaction, J. Phys. Chem. C 111 (2007) 16927–16933.
[52] D. Fernaíndez-Torre, K. Kosímider, J. Carrasco, M.V.N. Ganduglia-Pirovano, R.N. Peírez, Insight into the adsorption of water on the clean CeO_2 (111) surface with van der Waals and hybrid density functionals, J. Phys. Chem. C 116 (2012) 13584–13593.
[53] M.A. Henderson, C. Perkins, M.H. Engelhard, S. Thevuthasan, C.H. Peden, Redox properties of water on the oxidized and reduced surfaces of CeO_2 (111), Surf. Sci. 526 (2003) 1–18.
[54] G. Dutta, U.V. Waghmare, T. Baidya, M. Hegde, Hydrogen spillover on CeO $_2$/Pt: enhanced storage of active hydrogen, Chem. Mater. 19 (2007) 6430–6436.
[55] Y. Yeo, L. Vattuone, D. King, Calorimetric heats for CO and oxygen adsorption and for the catalytic CO oxidation reaction on Pt {111}, J. Chem. Phys. 106 (1997) 392–401.
[56] A. Mhadeshwar, D. Vlachos, Is the water–gas shift reaction on Pt simple?: Computer-aided microkinetic model reduction, lumped rate expression, and rate-determining step, Catal. Today 105 (2005) 162–172.
[57] C.-H. Lin, C.-L. Chen, J.-H. Wang, Mechanistic studies of water–gas-shift reaction on transition metals, J. Phys. Chem. C 115 (2011) 18582–18588.
[58] P. Norton, P. Richards, The heat of adsorption of hydrogen on platinum, Surf. Sci. 44 (1974) 129–140.
[59] J.A. Dumesic, The Microkinetics of Heterogeneous Catalysis, An American Chemical Society Publication, Washington D.C, 1993.
[60] A. Mhadeshwar, D. Vlachos, A thermodynamically consistent surface reaction mechanism for CO oxidation on Pt, Combust. Flame 142 (2005) 289–298.
[61] B. Bulfin, A. Lowe, K. Keogh, B. Murphy, O. Lübben, S. Krasnikov, I. Shvets, Analytical model of CeO_2 oxidation and reduction, J. Phys. Chem. C 117 (2013) 24129–24137.
[62] Y. Madier, C. Descorme, A.M. Le Govic, D. Duprez, Oxygen mobility in CeO_2 and $Ce_xZr_{(1-x)}O_2$ compounds: study by CO transient oxidation and 18O/16O isotopic exchange, J. Phys. Chem. B 103 (1999) 10999–11006.
[63] W. Tang, Z.P. Hu, M.J. Wang, G.D. Stucky, H. Metiu, E.W. McFarland, Methane complete and partial oxidation catalyzed by Pt-doped CeO_2, J. Catal. 273 (2010) 125–137.
[64] R. Tholkappiyan, K. Vishista, Influence of lanthanum on the optomagnetic properties of zinc ferrite prepared by combustion method, Phys. B 448 (2014) 177–183.
[65] L. Hu, P. Zhang, Y. Sun, S. Bao, Q. Chen, ZnO/Co_3O_4 porous nanocomposites derived from MOFs: room-temperature ferromagnetism and high catalytic oxidation of CO, ChemPhysChem 14 (2013) 3953–3959.
[66] D. Prusty, A. Pathak, M. Mukherjee, B. Mukherjee, A. Chowdhury, TEM and XPS studies on the faceted nanocrystals of $Ce_{0.8}Zr_{0.2}O_2$, Mater. Charact. 100 (2015) 31–35.
[67] M.H. Halabi, M.H.J.M. de Croon, J. van der Schaaf, P.D. Cobden, J.C. Schouten, Intrinsic kinetics of low temperature catalytic methane–steam reforming and water–gas shift over Rh/$Ce_\alpha Zr_{1-\alpha}O_2$ catalyst, Appl. Catal. A 389 (2010) 80–91.
[68] T. Ravikeerthi, R. Thyagarajan, N.S. Kaisare, P. Aghalayam, Microkinetic model for NOCO reaction: model reduction, Int. J. Chem. Kinet. 44 (2012) 577–585.
[69] T. Baidya, A. Gupta, P.A. Deshpandey, G. Madras, M. Hegde, High oxygen storage capacity and high rates of CO oxidation and NO reduction catalytic properties of Ce_{1-x} sn $_x$ O_2 and $Ce_{0.78}Sn_{0.2}Pd_{0.02}O_{2-\delta}$, J. Phys. Chem. C 113 (2009) 4059–4068.
[70] S. Roy, A. Marimuthu, M. Hegde, G. Madras, High rates of NO and N $_2$ O reduction by CO, CO and hydrocarbon oxidation by O $_2$ over nano crystalline Ce $_{0.98}$ Pd $_{0.02}$ O $_{2-\delta}$: catalytic and kinetic studies, Appl. Catal. B 71 (2007) 23–31.
[71] P. Singh, M.S. Hegde, $Ce_{1-x}Ru_xO_{2-\delta}$ (x = 0.05, 0.10): a new high oxygen storage material and Pt, Pd-free three-way catalyst, Chem. Mater. 21 (2009) 3337–3345.
[72] P. Singh, N. Mahadevaiah, S.K. Parida, M.S. Hegde, Ru4 + ion in CeO_2 ($Ce_{0.95}Ru_{0.05}O_{2-\delta}$): a non-deactivating, non-platinum catalyst for water gas shift reaction, J. Chem. Sci. 123 (2011) 577–592.